JACS
JOURNAL OF THE AMERICAN CHEMICAL SOCIETY
Article
pubs.acs.org/JACS

Improved Performances of Nanosilicon Electrodes Using the Salt LiFSI: A Photoelectron Spectroscopy Study

Bertrand Philippe,[†,‡,⊥] Rémi Dedryvère,*[,†,⊥,#] Mihaela Gorgoi,[§] Håkan Rensmo,[∥,⊥] Danielle Gonbeau,[†,⊥,#] and Kristina Edström*[,‡,⊥]

[†]IPREM/ECP (UMR 5254), University of Pau, Hélioparc, 2 av. Pierre Angot, 64053 Pau cedex 9, France
[‡]Department of Chemistry−Ångström Laboratory, Uppsala University, Box 538, SE-75121 Uppsala, Sweden
[∥]Department of Physics and Astronomy, Uppsala University, Box 516, SE-75121 Uppsala, Sweden
[§]Helmholz-Zentrum Berlin für Materialien und Energie GmbH, 12489 Berlin, Germany
[⊥]Alistore-European Research Institute, 33 rue Saint-Leu, 80039 Amiens cedex, France
[#]Réseau sur le Stockage Electrochimique de l'Energie (RS2E), FR CNRS 3459, France

Supporting Information

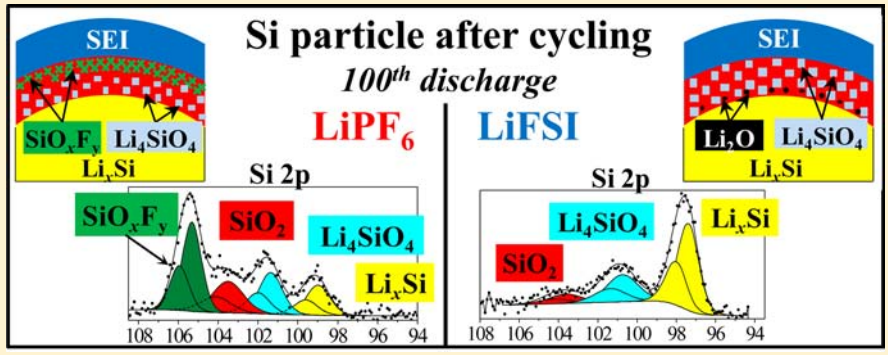

ABSTRACT: Silicon is a very good candidate for the next generation of negative electrodes for Li-ion batteries, due to its high rechargeable capacity. An important issue for the implementation of silicon is the control of the chemical reactivity at the electrode/electrolyte interface upon cycling, especially when using nanometric silicon particles. In this work we observed improved performances of Li//Si cells by using the new salt lithium bis(fluorosulfonyl)imide (LiFSI) with respect to $LiPF_6$. The interfacial chemistry upon long-term cycling was investigated by photoelectron spectroscopy (XPS or PES). A nondestructive depth resolved analysis was carried out by using both soft X-rays (100−800 eV) and hard X-rays (2000−7000 eV) from two different synchrotron facilities and in-house XPS (1486.6 eV). We show that LiFSI allows avoiding the fluorination process of the silicon particles surface upon long-term cycling, which is observed with the common salt $LiPF_6$. As a result the composition in surface silicon phases is modified, and the favorable interactions between the binder and the active material surface are preserved. Moreover a reduction mechanism of the salt LiFSI at the surface of the electrode could be evidenced, and the reactivity of the salt toward reduction was investigated using *ab initio* calculations. The reduction products deposited at the surface of the electrode act as a passivation layer which prevents further reduction of the salt and preserves the electrochemical performances of the battery.

1. INTRODUCTION

Since the commercialization of the first Li-ion battery by Sony[1] in 1991, a lot of work has been done to improve their performance (reversible capacity, energy density, power, and safety). A huge variety of new electrode materials and electrolytes has emerged as potential replacements for the commercially used graphite (negative electrode), the cobalt-containing layered transition-metal oxides (positive electrode), and the widely used electrolyte lithium hexafluorophosphate ($LiPF_6$) in nonaqueous carbonate solutions.[2,3]

In the development of the negative electrode, one of the main objectives is to obtain higher capacity. The current graphitic carbon has a theoretical specific capacity of 372 mAh/g which corresponds to the intercalation of one lithium atom per six carbon atoms (LiC_6). The use of materials that are able to accommodate much more lithium in their structures by forming an alloy with lithium (Li_xM) is one direction taken by scientists. Several metals and semimetals (e.g., Si, Ge, Sn, Sb, etc.) present this ability. The formation of a lithium-rich alloy gives materials with high volumetric and

Received: March 27, 2013
Published: June 13, 2013

gravimetric capacities, and they also have a low working potential vs Li^+/Li.[4]

A good candidate for the next generation of batteries has to be abundant, environmentally friendly, cheap and safe; silicon fulfills these conditions. Silicon, which represents the second most abundant element in the earth's crust is a light element and can accommodate 3.75 Li atoms per Si atom at room temperature, resulting in a maximum capacity of 3579 mAh/g.

However, electrochemical cells using silicon are still suffering from a low Coulombic efficiency and a constant decrease in capacity. The main reason is due to the large volume expansion occurring upon lithiation of the silicon. Successive expansions/contractions of the Si particles can lead to cracking, partial, and/or full disconnection between the Si particles, the conductive additive (carbon black), and the current collector, and a part of the active material will thus be lost. A lot of different strategies have allowed to improve the stability of the cells by avoiding or limiting this volume expansion by, for example, reducing the size of the particles,[5] by using specific cycling conditions of the battery,[6] and more recently, by the development of nanostructured Si materials.[7−13]

An additional reason for the observed irreversible capacity is the result of the electrolyte decomposition and the formation of a protective film: the solid electrolyte interphase (SEI). For Si-based electrodes, the formation of the SEI is affected by cracks during the volume expansion/contraction during cycling, and it has to be continuously reformed consuming extra amounts of lithium. The stability of the SEI layer is crucial for maintaining good performance of a Li-ion battery.

To improve the stability of the SEI layer, electrolyte additives such as VC,[14] FEC,[15,16] or silanes[17,18] have been added to the classical electrolyte ($LiPF_6$ in nonaqueous carbonate solvents, e.g. EC, DEC, dimethyl carbonate (DMC)).

However, the role of the electrolyte salt itself and its interface reactivity have attracted less attention and in the current Li-ion batteries, it is $LiPF_6$ which is used as conducting salt. This salt presents a high ionic conductivity and good electrochemical stability when it is solved in carbonate solvents; alicyclic (e.g., EC and PC) and linear carbonates (e.g., DMC, DEC, EMC). Compared to the historically used salts, i.e., $LiAsF_6$, $LiClO_4$, $LiBF_4$, $Li(SO_3CF_3)$ (LiTf), or the imide $LiN(SO_2CF_3)_2$ (LiTFSI) and its derivative $Li[N(SO_2C_2F_5)_2]$ (LiBETI),[19,20] $LiPF_6$ was reported to be the best salt. All the other classical salts are suffering from different weaknesses: the toxicity of $LiAsF_6$, the low ion conductivity of $LiBF_4$, the risk of violent reactions with $LiClO_4$, and finally the corrosion of the aluminum current collector when LiTf or LiTFSI is used.[21]

Nevertheless, $LiPF_6$ is not the perfect salt and presents many problems. It is well-known that it is thermally instable and also extremely sensitive to traces of water, moisture and alcohol[22,23] leading to the formation of hydrofluoric acid HF.[24,25] Additionally, the risk of release of gaseous HF in case of thermal runaway of the battery presents a safety problem that needs to be solved. Therefore the replacement of the classical $LiPF_6$ salt has to be considered.

In the case of a silicon-based electrode, the etching of the silicon oxide layer at the surface of the particles by HF can modify the favorable interactions between the binder and the active material surface and may explain the capacity fading upon long-term cycling.[26,27] As shown in our previous work, fluorinated species SiO_xF_y are irreversibly formed at the surface of the silicon particles upon long cycling due to reaction of the surface oxide with HF.[28]

Recently, other new imides salts have emerged, such as $Li[N(SO_2CF_3)(SO_2C_4F_9)]$[29] (LiTNSI) or Li[N(SO2F)(SO2-*n*-C4F9)] (LiFNSFI),[30] but the large size of these molecules have shown negative impact on the conductivity of the electrolyte. Instead, successful tests of smaller and lighter imide salts than LiTFSI have been carried out. One of the most successful is lithium bis(fluorosulfonyl)imide $Li[N(SO_2F)_2]$ (LiFSI).

The FSI^- anion is commonly used in ionic liquids (ILs).[31−33] Recently, some studies have shown that in gel polymer electrolytes[34] or in carbonates-based liquid electrolytes,[35,36] LiFSI presents a better ionic conductivity than $LiPF_6$, suggesting that it can be used as lithium salt in nonaqueous electrolytes for Li-ion batteries. LiFSI shows good anticorrosive properties toward aluminum, especially when a salt of high purity is used.[36,37] LiFSI outperforms $LiPF_6$ and exhibits good electrochemical performances when used as salt in nonaqueous carbonates solvents in half-cells: Li//$LiFePO_4$,[33,35] Li//$LiCoO_2$,[36] Li//graphite,[33,35] or in the full graphite//$LiCoO_2$ cell.[36] The better stability toward hydrolysis than $LiPF_6$ is another advantage of LiFSI, which can be a crucial point for the good cyclability of lithium-ion batteries.[36]

In the present study, we have investigated the electrochemical performances of nano silicon-based electrodes using LiFSI as conductive salt with respect to $LiPF_6$. We followed the evolution of the Li−Si alloy, of the surface oxide and other interfacial phases, and of the passivation layer (SEI) upon long-term cycling with photoelectron spectroscopy (PES or XPS). It is one of the few techniques that can give detailed chemical information of a few nanometers thick surface layers, which is necessary in this kind of study. Especially, it was shown that the nature of the salt may have an influence on the thickness and chemical composition of the SEI.[38−40] In the present paper we carried out a nondestructive depth-resolved analysis by changing the photon energy (instead of using the surface destructive argon-ion etching). The electrodes were studied by both soft X-ray PES (photon energy $h\nu$ = 100−800 eV) and hard X-ray PES (HAXPES, $h\nu$ = 2000−7000 eV) at two different synchrotron facilities (MaxIV Laboratory, Lund, Sweden; and Bessy II, Helmholtz Centre, Berlin, Germany) as well as by the use of in-house PES (Al Kα = 1486.6 eV).

The last part of the paper will be devoted to the discussion of LiFSI decomposition mechanisms with the help of *ab initio* calculations.

2. EXPERIMENTAL DETAILS

2.1. Electrochemical Cycling. Silicon electrodes were prepared with a mixture of 80% (wt %) of crystalline silicon powder (~50 nm, Alfa Aesar), 12% of conductive additive carbon black (SuperP, Erachem Comilog), and 8% binder of sodium carboxymethyl cellulose (CMC, M_w = 700.000, DS = 0.9, Sigma Aldrich). A water−ethanol solution ($EtOH/H_2O$, 70/30) was used as solvent for the slurry preparation. The slurry was mixed in a Retsch planetary mill for 60 min and deposited on a 20 μm thick copper foil. It was then dried at 60 °C for 12 h in an oven, and the obtained coating had a thickness of ~12−13 μm. Circular electrodes (2 cm diameter) were punched out and dried for 8 h at 120 °C in a vacuum furnace inside the argon glovebox (O_2 < 3 ppm, H_2O < 1 ppm).

Electrochemical cells were assembled by stacking the Si/C/CMC composite electrode (working electrode), a lithium foil (counter and reference electrode), and a polymer separator soaked with the electrolyte made up of 1 M $LiPF_6$ or 1 M LiFSI (Suzhou Fluolyte Co., purity >99.9%, H_2O < 50 ppm, Cl^- <1 ppm, SO_4^{2-} < 1 ppm) dissolved in a mixture of ethylene carbonate (EC) and diethyl carbonate (DEC) (2:1 (v/v), Novolyte Purolyte). Karl Fischer

dx.doi.org/10.1021/ja403082s | J. Am. Chem. Soc. 2013, 135, 9829−9842

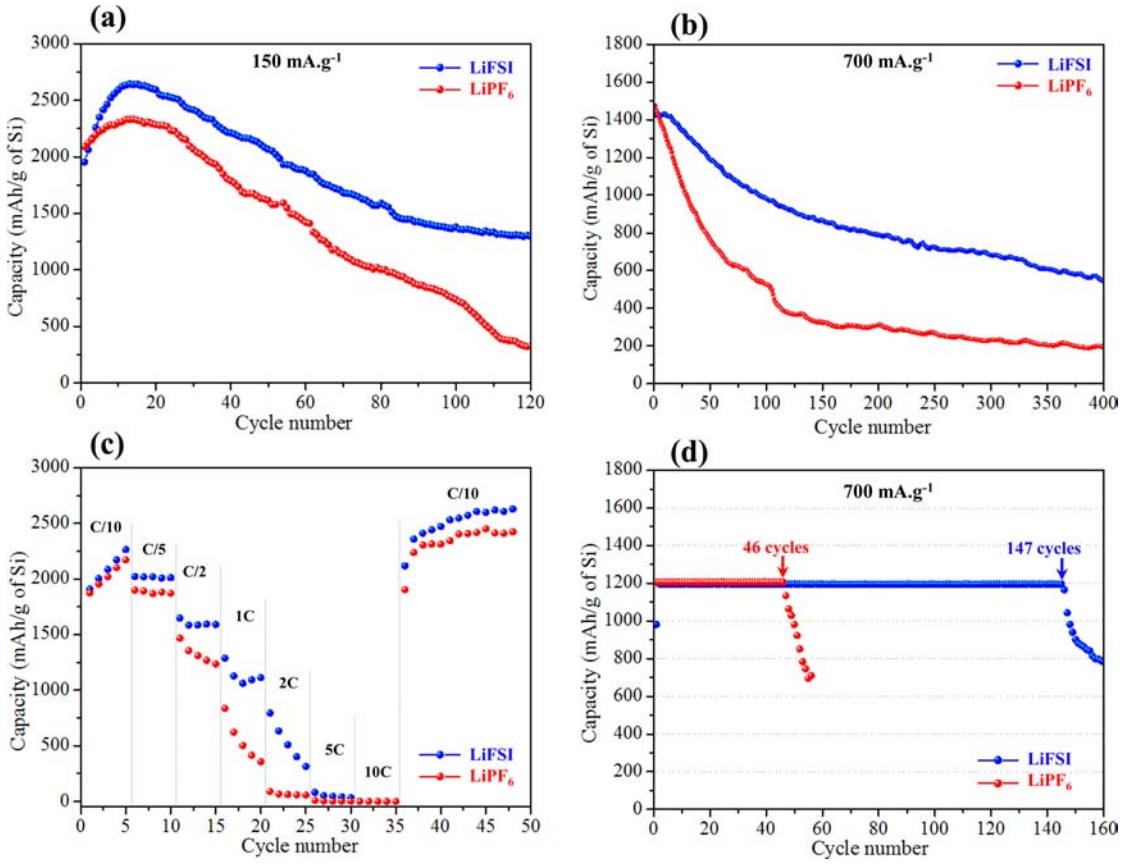

Figure 1. Electrochemical tests of Li//Si cells using either LiFSI (in blue) or $LiPF_6$ (in red) salts. (a,b) Discharge capacity vs cycle number upon galvanostatic cycling between 0.12 and 0.9 V at current rates of 150 and 700 $mA{\cdot}g^{-1}$ of Si (precycling is not shown). (c) Discharge capacities vs cycle number at different current rates from C/10 to 10 C (rate capability test). (precycling is not shown). (d) Fixed capacity test. The discharge capacity was limited to 1200 $mAh{\cdot}g^{-1}$ of Si (see text).

titration showed the water content to be below 10 ppm (the detection limit of the instrument). This assembly was hermetically vacuum sealed in a polyethylene-coated aluminum bag with attached nickel tabs as current collectors.

2.1.1. Standard Galvanostatic Cycling. The cell experiments were galvanostatically performed using an Arbin Instrument BT-2043 multichannel testing apparatus at a constant current of 150 or 700 mA per gram of silicon between 0.12 and 0.9 V.

2.1.2. Rate Capability Tests. The cells used for the rate capability experiments were cycled successively at constant current rates of 150, 300, 750, 1500, 3000, 7500, 15 000, and 150 $mA{\cdot}g^{-1}$ of silicon with 5 cycles at each rate. These current rates correspond to C/10, C/5, C/2, C, 2C, 5C, 10C, and C/10, respectively, where C/10 means that the theoretical gravimetric capacity of silicon when it is cycled between 0.12 and 0.9 V, i.e., 1500 $mAh{\cdot}g^{-1}$, is reached in 10 h.

Four precycles were performed prior to standard galvanostatic cycling and rate capability tests. In the four precycles, the electrodes were successively discharged to gravimetric capacities of 500, 1000, 1500, and 2000 $mAh{\cdot}g^{-1}$ and charged up to a 0.9 V potential.[41] During this step, the initial crystalline structure is slowly transformed into an amorphous phase. For standard galvanostatic cycling, the 0.12 V discharge cutoff voltage allows a capacity limitation in order to reduce the volume expansion of the Si particles. Hence, both the binder and the porosity of the electrode can accommodate the expansion. The second advantage is to avoid the formation of the crystalline phase $Li_{15}Si_4$.[42]

2.1.3. Fixed Capacity Test. The last cycling experiment was performed at a current rate of 700 $mA{\cdot}g^{-1}$ of silicon. The discharge was limited by a capacity of 1200 $mAh{\cdot}g^{-1}$ or a cutoff voltage of 0.005 V, whichever occurs first.[43] The charge was limited by a cutoff voltage of 1.0 V. No precycling was performed for this study.

After cycling the voltage was fixed for 1 h to allow relaxation of the cell. The cell was then disconnected, and the current connectors were protected by an adhesive tape to avoid short-circuit during transportation.

Before each PES characterization, the silicon electrode was carefully separated from the rest of the battery components in an argon glovebox at the syncrhotrons (O_2, H_2O < 1 ppm) and washed with DMC solvent in three successive baths to remove the electrolyte. For each bath, the electrode was put into 2 mL of ultralow water content DMC in a clean and dry aluminum container, maintaining a mild manual agitation during 1 min. Then the electrode was removed from the container, quickly dried (procedure repeated three times), and then mounted on a special built sample holder for PES analysis containing the same atmosphere as in the glovebox.

2.2. X-ray Photoelectron Spectroscopy. Careful precautions were taken for all XPS experiments in order to avoid moisture/air exposure of samples during transfer. Samples were either transferred directly from the argon glovebox to the in-house spectrometer or via an especially designed stainless steel transfer system at the synchrotron facility PES end-stations. The stainless steel transfer system was directly connected to the glovebox and allowed transportation of the sample from the glovebox to the introduction chamber of the spectrometer avoiding air contamination. The binding energy (BE) scale was calibrated with the hydrocarbon C 1s peak at 285.0 eV.

2.2.1. In-House XPS. The measurements were carried out with a Thermo Scientific K-Alpha spectrometer using a focused monochromatized Al Kα radiation ($h\nu$ = 1486.6 eV) operating at 72 W. The analyzed area of the samples was a 400 μm diameter disk. The pressure in the analysis chamber was around 1.10^{-7} mbar. Short-time spectra were recorded before and after each normal long-time experiment and were compared to each other to check that the samples did not suffer

dx.doi.org/10.1021/ja403082s | J. Am. Chem. Soc. 2013, 135, 9829−9842

from degradation during the measurements. Core peaks were analyzed using a nonlinear Shirley-type background,[44] and peak positions and areas were obtained by a weighted least-squares fitting of model curves (70% Gaussian and 30% Lorentzian combination). Quantification was performed on the basis of Scofield's photoionization cross sections.[45]

2.2.2. Soft X-ray PES. Soft X-ray PES measurements were carried out at the MaxIV Laboratory synchrotron facility (I-411 beamline, National Synchrotron Radiation Laboratory, Lund, Sweden), where the usable photon energies range from 50 to 1500 eV. Photons were monochromatized by a Zeiss SX-700 plan grating monochromator. The photoelectron kinetic energies (KE) were measured using a Scienta R4000 WAL analyzer. In order to have the same analysis depth for all spectra recorded with soft X-rays, the same photoelectron KE 130 eV was used for all probe elements. No charge neutralizer was used during the measurements. The pressure in the analysis chamber was about 10^{-8} mbar.

2.2.3. Hard X-ray PES. Hard X-ray PES measurements were carried out at BESSY II synchrotron facility (HIKE end station,[46] KMC-1 beamline,[47] Helmholtz Zentrum Berlin, Germany), where the usable photon energies range from 2000 to 10 000 eV. Fixed excitation energies were used, namely 2300 and 6900 eV (first-order lights from respectively Si(111) and Si(422) of the double-crystal monochromator). Note that a specific energy of 2200 eV (instead of 2300 eV) was used for F 1s spectra to avoid overlapping with Si $KL_{2,3}L_{2,3}$ Auger peak (KE ∼ 1618 eV).

The analyzer was a Scienta R4000 optimized for high kinetic energies up to 10 keV. No charge neutralizer was used, and the pressure was around 10^{-8} mbar in the analysis chamber during the measurements.

2.3. Computational Details. *Ab initio* calculations were carried out to determine the monoelectronic energy levels and the molecular orbitals (MOs) of FSI^- ion, in order to interpret and simulate the XPS valence spectrum of LiFSI using the Koopman's theorem approximation and to discuss its chemical reactivity from the analysis of the highest occupied and the lowest unoccupied molecular orbitals (HOMO and LUMO). Calculations were carried out at the DFT/B3LYP[48] level using Gaussian 09 program package[49] and the standard 6-311G* basis set. Representation of MOs was done using Molekel 5.4 software.[50]

The intensities of the XPS valence spectrum were estimated using the Gelius intensity model,[51−53] which is based on the assumption that the photoionization cross-section of a MO is determined by the cross sections of the corresponding atomic orbitals (AOs) in the LCAO model. According to this model, the intensity of the j^{th} MO is given by eq 1:

$$I_j \propto \left(1 - \frac{3\cos^2\theta - 1}{4}\beta_j\right) \sum_{i\mathrm{AO}} P_{j,i}\sigma_i \qquad (1)$$

where θ is the angle between the incoming unpolarized photon direction and the emitted photoelectrons direction, β_j is an asymmetry factor ($-1 \le \beta_j \le 2$), $P_{j,i}$ is the electron population of the i^{th} AO for the j^{th} MO, and σ_i is the atomic photoionization cross-section relating to the i^{th} AO.

For each MO, the weighted sum is extended over all the valence AOs using Scofield's atomic photoionization cross sections.[45] The term ($3\cos^2\theta - 1$) vanishes for the "magic angle" $\theta = 54.74°$. The geometry of the in-house XPS spectrometer used in this work corresponds to $\theta = 55°$, so the term containing the molecular asymmetry parameter β_j can be neglected. Thus, eq 1 can be simplified into eq 2:

$$I_j \propto \sum_{i\mathrm{AO}} P_{j,i}\sigma_i \qquad (2)$$

Simulated XPS valence spectra were calculated from the monoelectronic energy levels ε_j, and the intensities I_j calculated for each MO. They consist of a series of peaks centered at the monoelectronic energies ε_j. In order to obtain a simulation closer to the experiment, each peak was represented by a functional shape made of a combination of Gaussian and Lorentzian profiles (70% Gaussian, 30% Lorentzian). This method was successfully employed for other lithium salts ($LiPF_6$, $LiBF_4$, LiTFSI, and LiBETI) in a previous work.[54]

3. RESULTS AND DISCUSSION

3.1. Electrochemical Results. Figure 1 shows the electrochemical performances of Li//Si cells using either LiFSI (in blue) or $LiPF_6$ (in red) salts. All Si/C/CMC composite electrodes arose from the same batch, so the only difference is the salt of the electrolyte.

Figure 1a,b shows the discharge capacity vs cycle number upon galvanostatic cycling between 0.12 and 0.9 V at current rates of 150 and 700 $mA{\cdot}g^{-1}$ of Si. At the lowest rate, the discharge capacity of the first cycle (after the four precycles) is around 2000 $mAh{\cdot}g^{-1}$ with both salts (1960 $mAh{\cdot}g^{-1}$ with LiFSI, 2090 $mAh{\cdot}g^{-1}$ with $LiPF_6$). After 15 cycles, the capacity increases up to 2640 and 2330 $mAh{\cdot}g^{-1}$ for LiFSI and $LiPF_6$, respectively. Then it decreases gradually for both salts, but the capacity fading is much weaker with LiFSI. After 120 cycles the obtained capacity is ∼300 $mAh{\cdot}g^{-1}$ with $LiPF_6$ and 1300 $mAh{\cdot}g^{-1}$ with LiFSI. In other words, 66% of the initial discharge capacity is retained using LiFSI salt whereas only 16% with $LiPF_6$ after 120 cycles.

At higher rate (Figure 1b) the discharge capacity of the first cycle is lower for both salts (about 1400−1500 $mAh{\cdot}g^{-1}$), and the capacity fading upon cycling is greater. However, the capacity retention is much better with LiFSI salt, which allows maintaining 66% of the initial capacity after 100 cycles and 37% after 400 cycles, whereas the capacity retention with the common salt $LiPF_6$ is only 35% after 100 cycles and 13% after 400 cycles. We can thus clearly state that LiFSI sustains more stable discharge capacities than $LiPF_6$ upon long-term cycling for both current rates.

Figure 1c shows discharge capacities vs cycle number of Li//Si cells at different current rates from C/10 to 10 C (rate capability test). The discharge capacities of the first cycle are similar for both salts (∼1900 $mAh{\cdot}g^{-1}$). Upon the first five cycles at C/10 (150 $mA{\cdot}g^{-1}$), they increase up to 2200−2300 $mAh{\cdot}g^{-1}$. This increase is greater with LiFSI than with $LiPF_6$, in agreement with the capacity increase already observed in Figure 1a. A careful study of voltage vs capacity discharge/charge curves of the first cycles (not shown here, see Supporting Information) has shown that this capacity increase is not due to SEI formation/electrolyte decomposition but to the presence of remaining pristine silicon particles after the precycling step, which are being lithiated over the first following cycles. During the following steps at higher cycling rates, we can observe a significant decrease of the capacities as a function of the applied current, and for the highest rates, a rapid capacity fading as a function of the cycle number. However, we can notice that the rate capability is better with LiFSI than with $LiPF_6$.

When a low current rate is applied again (C/10), the initial capacities of 1900 $mAh{\cdot}g^{-1}$ (with $LiPF_6$) and 2100 $mAh{\cdot}g^{-1}$ (with LiFSI) are recovered. Then in the following cycles the capacity increases and stabilizes after 10 cycles at ∼2400 and 2600 $mAh{\cdot}g^{-1}$ with $LiPF_6$ and LiFSI, respectively. Such capacity recovery suggests that the electrode material is not significantly damaged during fast cycling with both salts. Finally, this electrochemical test clearly shows the better capacity retention at high current rate when LiFSI salt is used.

The last electrochemical test presented in Figure 1d compares the cycling performances of Li//Si cells when a limited discharge capacity is applied (1200 $mAh{\cdot}g^{-1}$), according to a test previously used by Oumellal et al.[43] When this capacity

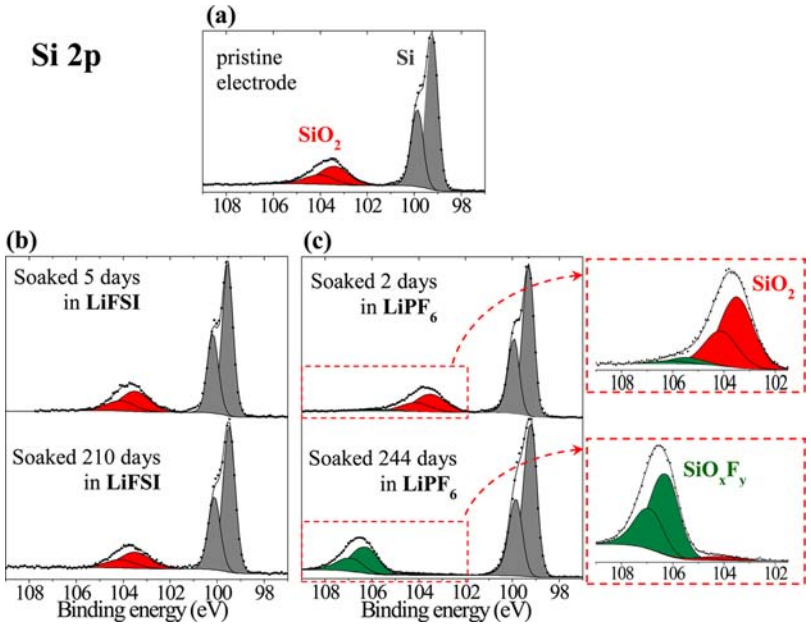

Figure 2. Si 2p spectra (in-house PES, hν = 1486.6 eV) of (a) the pristine Si electrode and after contact with an electrolyte containing either (b) LiFSI or (c) $LiPF_6$. A zoom of the 102−109 eV BE region is shown on the right for $LiPF_6$.

value cannot be reached anymore upon cycling, the discharge is limited by a 0.005 V cutoff voltage, and the capacity fades rapidly. We can see in Figure 1d that a 1200 $mAh{\cdot}g^{-1}$ capacity can be retained for 46 cycles with $LiPF_6$, whereas 147 cycles can be achieved using LiFSI.

It was previously shown in the literature that LiFSI outperforms $LiPF_6$ when used as salt in nonaqueous liquid electrolyte in both Li//$LiCoO_2$ and graphite//$LiCoO_2$ cells[35,36] In this study, we clearly show that the performances of a Li//Si cells are also better with LiFSI than with $LiPF_6$. The aim of this paper is now to understand why LiFSI allows improved performances. The bulk properties of LiFSI-based electrolytes may be of course involved. However, since the formation and evolution of electrode/electrolyte interfaces are a major factor governing the performances and stability of lithium-ion batteries, we will now focus our attention on the mechanisms occurring at the surface of the silicon electrodes by using photoemission spectroscopy, and the results will be compared with those previously obtained with $LiPF_6$.[28,55]

3.2. Reactivity of the Si Electrode toward the Electrolyte. The first step of the present study is to investigate the reactivity of the silicon electrode toward an electrolyte containing LiFSI with respect to an electrolyte containing the common salt $LiPF_6$. To this aim, Li//Si cells were mounted and stored without any electrochemical cycling and then opened, and the electrode was washed with DMC before XPS analysis.

Figure 2 shows the Si 2p core peak of: (a) the pristine Si/C/CMC electrode, after contact with an electrolyte containing either (b) LiFSI or (c) $LiPF_6$. In the spectrum of the pristine electrode we can observe a first peak assigned to bulk silicon (Si $2p_{3/2}$ at ∼99 eV, gray color) and another one assigned to the surface oxide SiO_2 (Si $2p_{3/2}$ at 103.5 eV, red color), due to the analysis depth lower than 10 nm.

After 5 and 210 days of contact of the silicon electrode with the electrolyte containing LiFSI, no difference can be observed. The SiO_2/Si area ratio remains constant and no additional peak appears, suggesting that the silicon particles surface did not react with the electrolyte.

Rather the opposite, after contact with the electrolyte containing $LiPF_6$ we could observe an additional component at higher BE (Si $2p_{3/2}$ at ∼106 eV, green color). The intensity of this component was very weak after two days but almost totally replaced the oxide component after 244 days, which can be explained by the formation of a partially fluorinated silicon species SiO_xF_y ($y \leq 3$) at the surface, as it was shown in a previous work.[28] The formation of such species is due to the reaction of surface oxide SiO_2 with hydrofluoric acid HF resulting from $LiPF_6$ hydrolysis by traces of water.[24] The absence of such fluorinated species at the surface of the silicon electrode after contact with the electrolyte containing LiFSI is consistent with the lower sensitivity of this salt toward hydrolysis than $LiPF_6$.[36]

3.3. Effect of Electrochemical Cycling on the Electrode Surface. *3.3.1. Evolution of Si Compounds.* In this work we carried out a nondestructive depth-resolved PES analysis by varying the photon energy of the incident beam at the synchrotron facility. An increase of the photon energy hν leads to an increase of the kinetic energy (KE) of the ejected photoelectrons for a given core level. Since the inelastic mean free path (IMFP) of the photoelectron depends on its KE, the PES analysis depth depends on the photon energy. Moreover, the use of high photon energies allows the extraction of electrons from deeper core levels, e.g. Si 1s with a BE around 1840 eV, which is not accessible from in-house XPS with hν = 1486.6 eV. Similar information is provided by Si 1s and Si 2p core levels, but at a given photon energy the analysis depths probed by these two core levels are different, Si 1s being more surface sensitive than Si 2p. Table 1 summarizes the variation of the KE as a function of the chosen Si core level and photon energy. The corresponding reported analysis depths were estimated according to the model developed by Tanuma et al.,[56] considering that 95% of the PES signal comes from a layer thickness equal to three times the IMFP. They range from about 4 nm for Si 1s at 2300 eV to about 27 nm for Si 1s at 6900 eV, which allows a characterization from the surface to the core of our ∼50 nm diameter Si particles.

dx.doi.org/10.1021/ja403082s | J. Am. Chem. Soc. 2013, 135, 9829−9842

Table 1. Photon Energies (hν) and Binding Energies of the Si Core Levels Used in This Work, with Corresponding Kinetic Energies[a]

Si core level photon energy hν	Si 1s 2300 eV	Si 2p 1486.6 eV	Si 2p 2300 eV	Si 1s 6900 eV
BE (eV)	1840	100	100	1840
KE (eV)	460	1386	2200	5060
analysis depth (nm)	4	9	14	27

[a]Analysis depths were estimated according to the model of Tanuma et al.[53]

Figure 3 shows the evolution of the Si 1s core peak of the silicon electrode upon the first discharge of a Li//Si cell using a

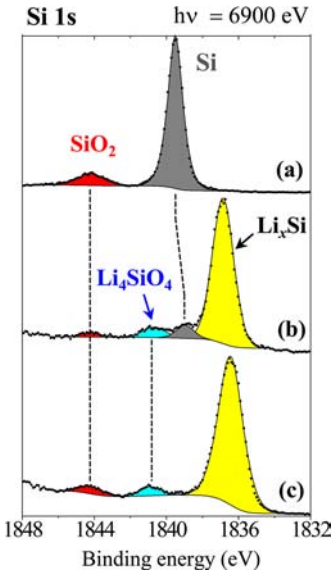

Figure 3. Evolution of Si 1s spectra of the silicon electrode upon the first discharge of a Li//Si cell with an electrolyte containing LiFSI (hν = 6900 eV, greatest analysis depth): (a) uncycled electrode (soaked 5 days in the electrolyte); (b) discharge at 0.06 V vs Li^+/Li; (c) full discharge (0.01 V vs Li^+/Li).

LiFSI-based electrolyte. The photon energy (hν = 6900 eV) corresponds to the greatest PES analysis depth of this study. For the pristine electrode the Si 1s spectrum is similar to Si 2p previously discussed in Figure 2, but the SiO_2/Si area ratio is smaller due to the greater analysis depth. After discharge down to 0.06 V, four peaks can be observed. The oxide peak at ∼1844 eV (red) is still observable, but its intensity has decreased due to the reduction of SiO_2 with lithium to form Si and Li_2O. The unreacted bulk silicon peak (gray) is very weak because it has been replaced by the Li−Si alloy peak at ∼1836 eV (yellow), following insertion of lithium into the electrode. Due to the great analysis depth, this peak is still easily observed, although unreacted silicon is located in the core of the particles. Moreover, a slight shift of the Si peak toward the lower BE is observed, as discussed in our previous work carried out with $LiPF_6$ salt.[55] An additional weak peak at ∼1841 eV (blue) can be attributed to the formation of the phase Li_4SiO_4 ensuing from the reaction of the surface oxide with Li, as evidenced in recent papers.[55,57,58] After full discharge down to 0.01 V, the bulk silicon peak has been totally replaced by the Li−Si alloy peak.

The evolution of Si 2p/Si 1s core peaks of the silicon electrode over 100 cycles of charge/discharge between 0.12 and 0.9 V is shown in Figure 4 (precycling is not shown). Data are sorted as a function of the photoelectron KE and thus of the analysis depth (see Table 1). Great differences are observed in the area ratios of the components attributed to the surface oxide SiO_2, the lithium silicate Li_4SiO_4, and the Li_xSi alloy. The components attributed to the surface phases, especially SiO_2 and also Li_4SiO_4, are enhanced by the lowest analysis depths (particularly for Si 1s with hν = 2300 eV), whereas the Li_xSi alloy component is enhanced by the greatest analysis depths (particularly for Si 1s with hν = 6900 eV). The component assigned to bulk silicon is not detected anymore.

After 50 and 100 cycles the main difference with respect to the first cycle is the gradual decrease of the SiO_2/Li_4SiO_4 area ratio, showing that the reaction of the surface oxide SiO_2 with lithium continues upon repeated cycles.

The most important result is that no additional component appears. The observation was quite different with $LiPF_6$ after 100 cycles, as shown in the bottom left corner of Figure 4. The main component of the spectra after long cycling was attributed to the fluorinated compound SiO_xF_y located at the surface of the particles.[55] The absence of this component after 100 cycles with LiFSI confirms that no reaction of the particles surface with HF occurs upon long cycling when this salt is used. This important difference concerning the chemistry of the silicon particles surface is certainly directly linked to the improved performances of Li//Si electrochemical cells using LiFSI salt.

Finally, we can also notice a slight increase of the binding energy of the Li_xSi alloy component upon cycling (about −1 eV after 100 cycles). This shift may be interpreted by a gradual decrease of the lithium content in the Li−Si alloy, which is related to the observed capacity fading upon cycling, as shown in Figure 1.

3.3.2. Evolution of Oxygenated Species. Figure 5 shows O 1s spectra of the uncycled Si electrode (i.e., soaked 5 days in the electrolyte) and after the 1st, 50th, and 100th discharges (i.e., lithiated state) and charges (i.e., delithiated state) recorded with a photon energy of 6900 eV. The spectrum of the uncycled electrode shows a maximum at ∼533 eV that can be mainly assigned to the surface oxide SiO_2 and to the CMC (carboxymethyl cellulose) used as binder; both have similar BE. Additional oxygenated species may be present at the surface as well, following the contact of the Si electrode with the electrolyte.

After cycling, the overall shape of O 1s spectra changes following the formation of the SEI and thus the deposition of many oxygenated species at the surface of the electrode. A precise assignment of O 1s components is rather difficult since the signatures of the various oxygenated species are gathered in a narrow BE range. However, it is possible to see that the maximum of the spectra shifts to a lower BE (532.0 eV) with respect to the uncycled electrode. This value is in good agreement with the formation of carbonates in the SEI.[59]

The overall shape of O 1s spectra is very stable over 100 cycles both in charge and discharge, suggesting that the composition of oxygenated species in the SEI does not change significantly.

The high photon energy hν = 6900 eV chosen here corresponds to the highest analysis depth (∼33 nm) and allows us to detect all oxygenated species, including those which are covered by the SEI, like Li_2O, SiO_2, and Li_4SiO_4. The component observed at a BE of 530.3 eV is in good agreement with lithium silicate Li_4SiO_4.[55]

dx.doi.org/10.1021/ja403082s | J. Am. Chem. Soc. 2013, 135, 9829−9842

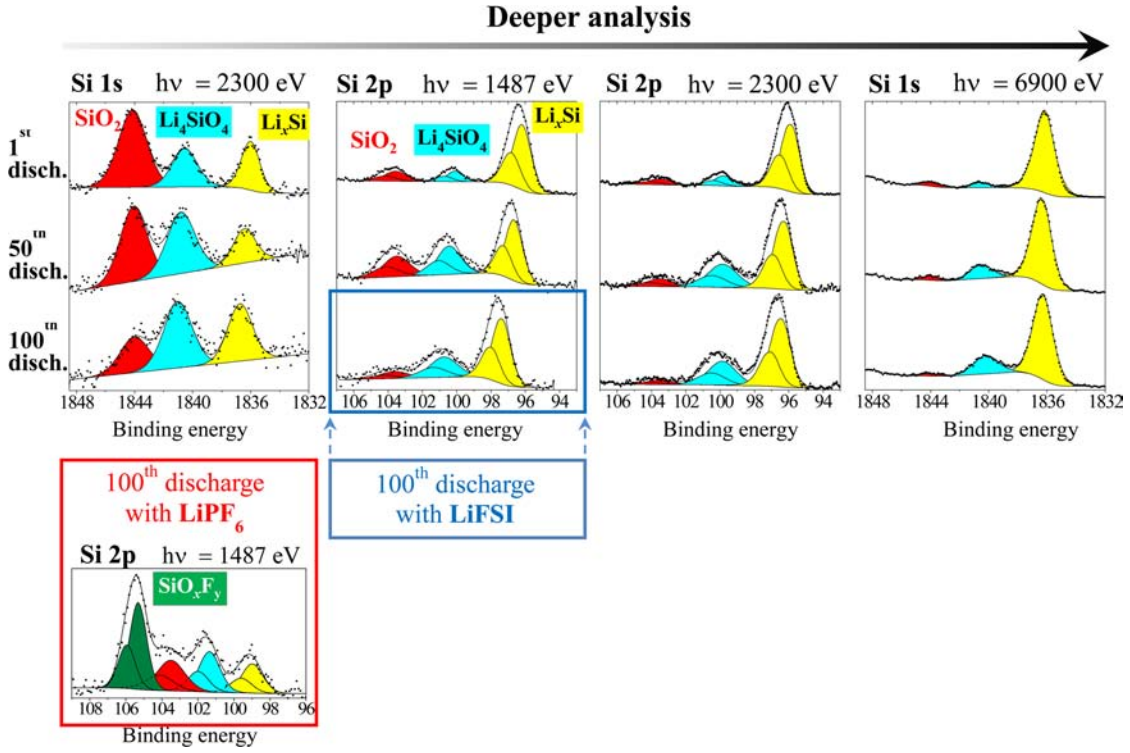

Figure 4. Evolution of Si 2p/Si 1s spectra of the Si electrode after the 1st, 50th, and 100th discharge of a Li//Si cell with an electrolyte containing LiFSI. Evolution as a function of the analysis depth. Comparison with the 100th discharge using $LiPF_6$ in the bottom left corner.[28].

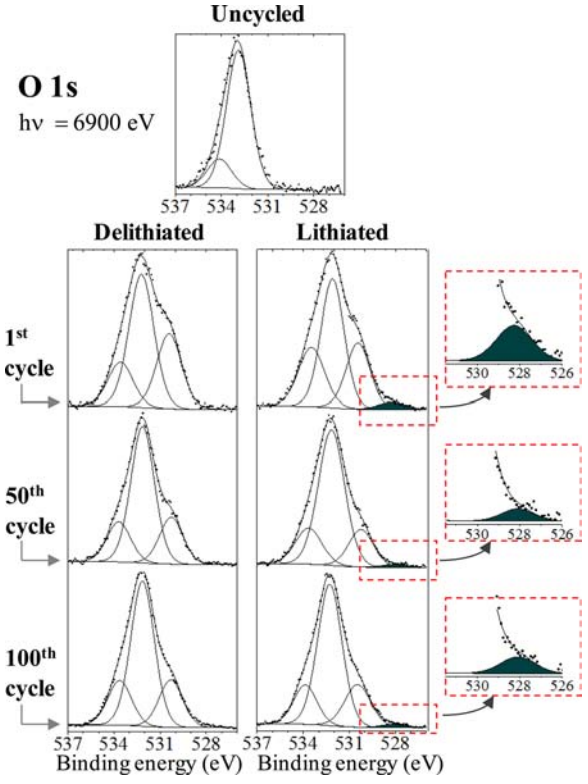

Figure 5. O 1s spectra of the Si electrode soaked 5 days in the electrolyte (uncycled), and after the 1st, 50th and 100th discharges (lithiated) and charges (delithiated) with an electrolyte containing LiFSI. A zoom of the low BE region is shown on the right to highlight the signature of Li_2O ($h\nu$ = 6900 eV).

Due to its characteristic O 1s signature with a very low binding energy of ~528 eV, Li_2O is easily detectable even when other oxygenated species are present in greater amount at the surface. We can see in Figure 5 that Li_2O can be detected in the lithiated state after the 1st, 50th, and 100th discharges (reduction), resulting from the reduction of the surface oxide by lithium: $SiO_2 + 4\ Li \rightarrow Si + 2\ Li_2O$. It is not detected anymore in the delithiated state after the 1st, 50th, and 100th charges (oxidation), showing the reversibility of its formation.

The situation was different with $LiPF_6$ after long cycling. Indeed, Li_2O still could be detected in the lithiated state after the 10th discharge, but no more after the 50th and 100th discharges.[28] This could be explained by the role of HF, which as an acid reacts with the basic Li_2O, in good agreement with the simultaneous appearance of SiO_xF_y species at the surface of the particles ensuing from the reaction of HF with SiO_2.

The present results show that after 100 discharges with LiFSI, lithium oxide is still detected. This is consistent with the lower sensitivity of this salt toward hydrolysis and the lower content of HF in the electrolyte.

Figure 6 summarizes these results and gives a comparison of the mechanisms occurring at the surface of a Si nanoparticle upon cycling when using either $LiPF_6$ or LiFSI salts. Upon the first discharge for both salts, Li reacts with the SiO_2 layer to form Li_2O and Li_4SiO_4 at the surface of the particles and with Si to form the Li_xSi alloy deeper inside. An SEI layer is formed at the surface of the particles. Upon long-term cycling, differences are observed. With $LiPF_6$ the presence of HF leads to the disappearance of Li_2O from the surface and to the appearance of fluorinated species SiO_xF_y due to reaction with SiO_2. The use of LiFSI prevents the formation of HF and, as a consequence, prevents the formation of fluorinated species SiO_xF_y at the surface of the Si particles. The reaction of SiO_2 with Li to form the silicate Li_4SiO_4, which is observed upon the first cycle,

dx.doi.org/10.1021/ja403082s | J. Am. Chem. Soc. 2013, 135, 9829−9842

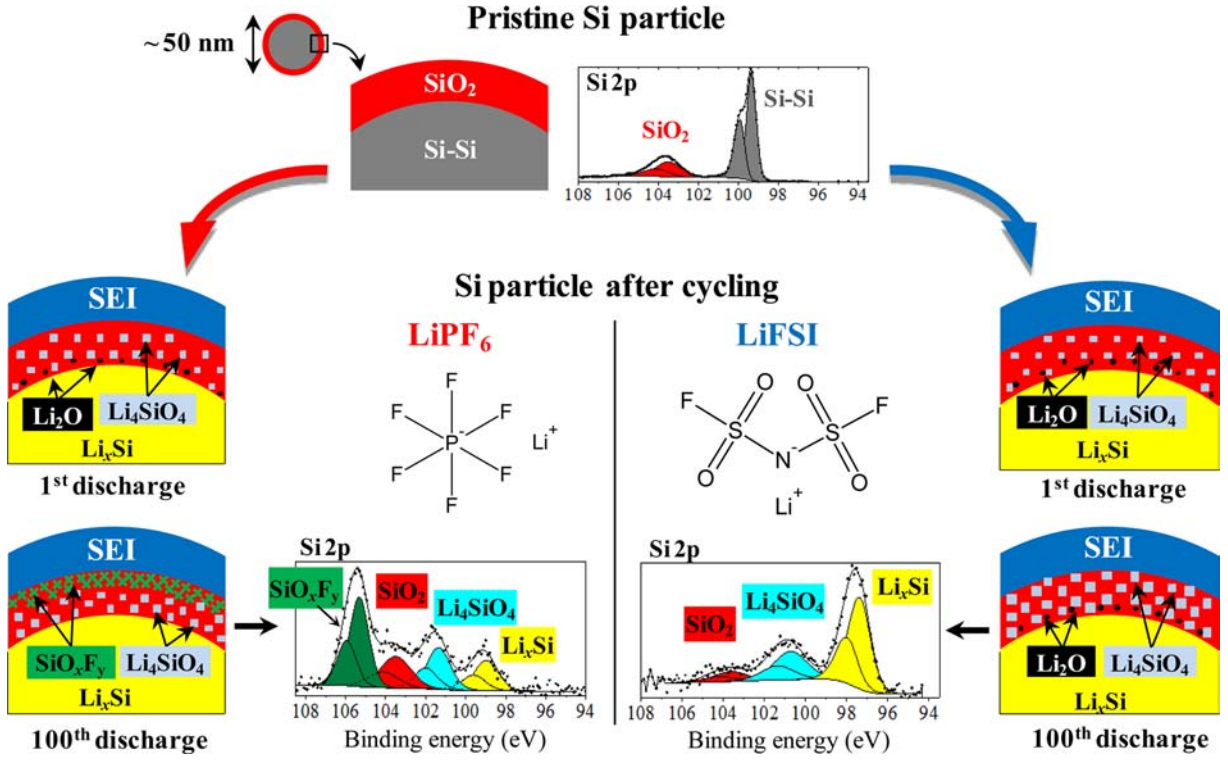

Figure 6. Schematic comparison of the mechanisms occurring at the surface of a silicon nanoparticle upon cycling of a Li//Si cell using either $LiPF_6$ or LiFSI salts.

continues over repeated cycling and leads to a decrease of the SiO_2/Li_4SiO_4 ratio after 100 cycles. These different mechanisms result in different particles surface chemistries and in different interactions between the active material particles and the other electrode components (binder, conductive carbon, current collector). It could also be related to different surface layers formed on the lithium counter electrode. Therefore we assume that these differences are some of the origins of the better electrochemical behavior of Li//Si cells using LiFSI with respect to $LiPF_6$.

We will now focus our discussion on the formation of the SEI.

3.3.3. Study of the SEI. 3.3.3.1. Covering Process. Figure 7 shows the evolution of the amount of silicon measured at the surface of the electrodes by in-house XPS ($h\nu$ = 1486.6 eV) after the 1st, 10th, 50th, 100th, and 1000th cycles (discharge down to 0.12 V and charge up to 0.9 V, after the precycling step) with respect to an uncycled electrode (soaked 5 days in the electrolyte).

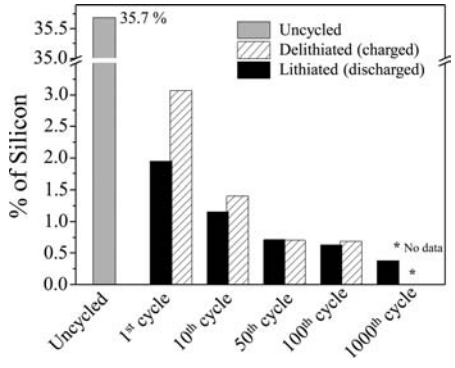

Figure 7. Evolution of atomic percentage of silicon measured at the surface of the electrodes (in-house XPS, $h\nu$ = 1486.6 eV) as a function of cycle number (after precycling). Charged (hatched) and discharged (black) states are differentiated.

All the phases containing silicon are located within the electrode and not in the SEI. Therefore when the electrode is covered by the SEI, the Si 2p signal of the electrode decreases, because of the XPS analysis depth (~5−10 nm in this case). The evolution of the atomic percentage of silicon is thus an indirect measurement of the SEI thickness (or more generally of the covering effect of the SEI because its thickness may be nonuniform).

We can observe in Figure 7 a dramatic decrease of the Si at. % from the uncycled electrode (35.7 at. %) to the cycled electrodes (~2 at. % of Si after the first discharge following the four precycles). This decrease results from SEI formation at the surface of the electrode. We can also observe a thickening of the SEI upon repeated cycling, but with some stabilization after 50 cycles (~0.4−0.7 at. % of Si between 50 and 1000 cycles). These results have the same order of magnitude as those obtained with $LiPF_6$ salt, but the thickness stabilization occurs as soon as the 10th discharge with $LiPF_6$.[28] Note that the SEI is slightly thinner after charge (delithiated state) than after discharge (delithiated state) at each cycle. This is due to a slight redissolution process of species of the SEI upon charge, leading to a kind of "breathing" of the SEI upon cycles.[60,61] This breathing effect fades upon long-term cycling.

3.3.3.2. Carbonaceous species of the SEI. Figure 8 shows C 1s spectra of the Si electrode after the 1st, 50th, and 100th discharges (i.e., lithiated state) with respect to the uncycled electrode (i.e., soaked 5 days in the electrolyte). Data are sorted as a function of the photon energy and thus of the analysis depth, from $h\nu$ = 1486.6−6900 eV.

dx.doi.org/10.1021/ja403082s | J. Am. Chem. Soc. 2013, 135, 9829−9842

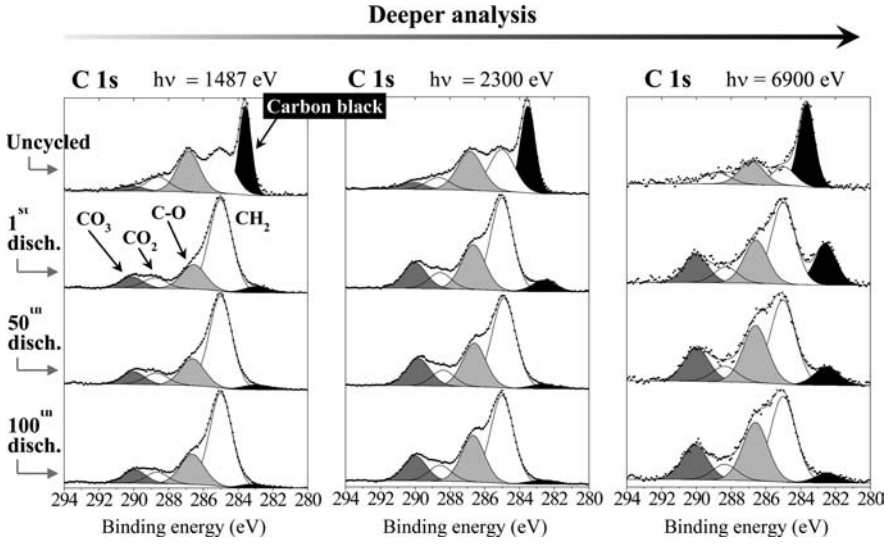

Figure 8. C 1s spectra of the Si electrode soaked 5 days in the electrolyte (uncycled) and after the 1st, 50th, and 100th discharges with an electrolyte containing LiFSI. Evolution as a function of the analysis depth.

The spectra of the uncycled electrode contain five components. The main and narrow peak with a binding energy at ∼283.5 eV (black) corresponds to carbon conductive additive. The component at 285.0 eV (white) is assigned to hydrocarbon surface contamination, always observed at the surface of a sample by PES. The two peaks at ∼286.5 and ∼288.5 eV (light gray and white, respectively) can be attributed to mono- and bioxygenated environments of carbon in CMC binder. Finally, the weak component at 290 eV (dark gray) can be attributed to carbonate resulting from the simple contact of the electrode with the electrolyte. As it is not detectable at the highest analysis depth ($h\nu$ = 6900 eV), this is a very thin carbonate layer adsorbed at the outermost surface.

After cycling, the intensity of the carbon black component decreases dramatically, especially for the lowest analysis depths ($h\nu$ = 1486.6 eV), because the surface of the electrode has been covered by the SEI which contains carbonaceous species. This decrease continues over 100 cycles (which is very clearly observed at 6900 eV) due to the gradual thickening of the SEI as a function of cycle number, in good agreement with Figure 7 discussed above.

New carbonaceous species have been deposited at the surface, and their characteristic peaks corresponding to CO (286.5 eV), CO_2 (288.5 eV), and CO_3 (290 eV) environments of carbon have masked the initial peaks of the uncycled electrode. Carbonaceous species with such carbon environments are commonly found in SEI layers formed with carbonate-based electrolytes,[39,61] and several formation mechanisms of such species have been described in the literature.[62−64]

At given photon energy, the ratio between CH_2, CO, CO_2, and CO_3 peaks is maintained from the 1st to the 100th discharge, showing the stability of the composition in carbonaceous compounds within the SEI layer upon cycling. For a given cycle number, the intensity of the CH_2 peak (285 eV) decreases when the photon energy increases, showing this peak is partly assigned to hydrocarbon contamination located at the outermost surface of the SEI. The ratio between CO, CO_2, and CO_3 peaks is independent of either the cycle number or the analysis depth. This result shows the stability of the chemical composition of the SEI upon cycling and its homogeneity from its outermost surface to its deeper layers.

3.3.3.3. Inorganic species of the SEI. To take into account the inorganic part of the SEI, it was first necessary to characterize LiFSI as pure salt (white powder). The characteristic BE (eV) from F 1s, O 1s, N 1s, S 2p, and Li 1s spectra of LiFSI are reported in Table 2. It was possible to fit F 1s, O 1s, N 1s, and Li 1s spectra with only one single component and S 2p spectrum with a sole doublet, all assigned to only one chemical environment. The obtained values for Li 1s, N 1s, and O 1s are rather close to those reported for $LiN(SO_2CF_3)_2$ (LiTFSI),[54] in which these elements have similar chemical environments, whereas the BE values for F 1s and S 2p are quite different (−0.7 eV for F 1s and +0.9 eV for S 2p) due to the presence of the S−F bond in LiFSI.

Table 2. Characteristic Binding Energies (eV) of LiFSI Salt[a]

LiFSI peak	BE (eV)
F 1s	687.9
O 1s	533.2
N 1s	400.0
S $2p_{3/2}$	170.3
Li 1s	56.8

[a]In house XPS, $h\nu$ = 1486.6 eV.

Figure 9 shows the evolution of S 2p, Si 2s, F 1s and N 1s spectra of the Si electrode from the uncycled electrode (soaked 5 days in the electrolyte) to the 1st, 50th, and 100th discharges. The presence of Si 2s and S 2p spectra in the same BE range, and especially the decrease of Si 2s/S 2p intensity ratio upon cycling, allow us to visualize the covering of the electrode surface by sulfur-containing species, i.e. by inorganic species of the SEI.

Note that the broad peak observed at 165−170 eV in the spectrum of the uncycled electrode corresponds to the Si 2s plasmon sideband of bulk silicon[65] and overlaps with S 2p, which hampers the analysis of sulfur when it is present in low amounts at the surface. After cycling, the Si 2s plasmon sideband of the Li-Si alloy is shifted toward lower BE (158−163

dx.doi.org/10.1021/ja403082s | J. Am. Chem. Soc. 2013, 135, 9829−9842

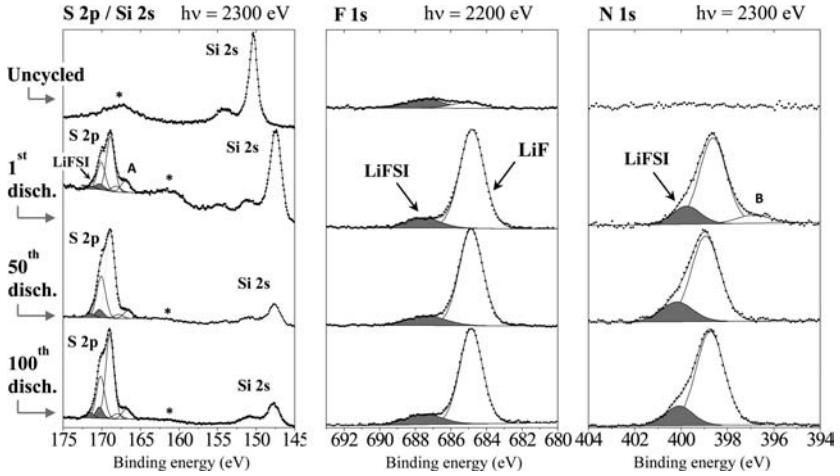

Figure 9. S 2p, Si 2s, F 1s and N 1s spectra of the Si electrode soaked 5 days in the electrolyte (uncycled), and after the 1st, 50th, and 100th discharges with an electrolyte containing LiFSI (* = Si 2s plasmon sidebands).

eV) and the global Si 2s intensity falls, so the S 2p spectrum can be easily analyzed.

After the 1st, 50th, and 100th discharges the S 2p spectrum of the electrode consists of 3 components. The main one (S $2p_{3/2}$ at 169 eV) cannot be attributed to LiFSI but to a degradation product of this salt. Actually the component assigned to LiFSI is still detectable but very weak (S $2p_{3/2}$ at 170.2 eV, gray in Figure 9) and allows us to evidence a degradation mechanism of the salt at the outermost surface of the electrode. The third and weak component at low BE (peak A at ∼167 eV) is also due to a degradation product of the salt but, since its intensity increases upon X-ray beam time exposure, it results from the PES analysis itself and not from the electrochemical cycling. Therefore it will not be considered.

We can notice that from the first to the 100th discharge, the intensity ratio of S 2p components does not change, and thus the salt degradation mechanism occurs in the early first cycles (precycling procedure).

The F 1s spectrum of the uncycled electrode shows two weak components. The F 1s signature of LiFSI salt can be recognized at 687.8 eV, and another component attributed to lithium fluoride LiF is observed at 685 eV, showing that a slight degradation mechanism of the salt occurs as soon as the simple contact of the electrode surface with the electrolyte.

After the 1st, 50th, and 100th discharges the F 1s peak of the salt becomes very weak, and the main component is LiF, showing the degradation mechanism induced by the electrochemical reaction at the surface of the electrode. Note this does not mean that the salt is degradated in the bulk electrolyte (the electrochemical performance of the cell would be lost), but that the SEI includes more degradation products of LiFSI than the salt itself. After 50 and 100 cycles the surface (i.e., the 5−10 nm thick layer analyzed by in-house XPS) consists of ∼10−11% of LiF.

The N 1s peak of the uncycled electrode could not be distinguished from the noise because the N 1s photoionization cross section at $h\nu$ = 2300 eV is about 2.5−3 times lower than F 1s.[66] After the 1st, 50th and 100th discharges the N 1s spectrum of the electrode consists of three components. The main one at ∼398.7 eV corresponds to an undefined degradation product of the salt. The component assigned to LiFSI is rather weak (N 1s at 400 eV, gray in Figure 8), confirming the degradation mechanism discussed above. The third weak component at low BE (peak B at ∼397 eV) is a degradation product induced only by X-ray beam exposure, since its intensity increases upon time during PES analysis. Therefore it will not be considered. From the 1st to the 100th discharge, the intensity ratio of N 1s components does not change, which confirms observations from S 2p and F 1s spectra.

As a summary, the intensity ratios between the characteristic peaks of organic and inorganic species making up the SEI are independent of the cycle number, which shows the stability of its chemical composition upon cycling (at least after the precycling step). Concerning the inorganic part, we have shown that it mainly consists of degradation compounds of the salt and that the ratio between LiFSI and its degradation compounds does not change upon cycling. In the following part, we will focus our study on the degradation mechanisms of the salt at the surface of the electrode.

3.4. Reactivity of LiFSI toward the Electrode Surface.

3.4.1. PES Study of the First Discharge. According to the results shown above, the degradation mechanism of the salt appears to occur in the early steps of the electrochemical reaction. Therefore, we now focus our study on the first discharge of a Li//Si cell (without any precycling) to follow the formation of inorganic species making up the SEI at the surface of the Si electrode at this early step.

Due to the very low thickness of the SEI at the first steps of the electrochemical reaction and to avoid overlapping of the Si 2s plasmon sideband with S 2p spectrum, we carried out this study by using soft X-rays ($h\nu$ = 300−810 eV), with a fixed photoelectron kinetic energy of 130 eV which allows a very low analysis depth (∼1−2 nm).

Figure 10 shows the evolution of F 1s, S 2p, and N 1s spectra of the Si electrode from the uncycled electrode (soaked 10 days in the electrolyte) to 0.5 and 0.1 V at the first discharge. The analyzed samples are highlighted by gray points in the electrochemical curve. Due to the very low analysis depth, the F 1s, S 2p, and N 1s PES spectra of the uncycled electrode are clearly exploitable. They all show the presence of the salt LiFSI (gray component in Figure 10) accompanied by a degradation product: F 1s spectrum shows the presence of LiF at 685 eV, whereas S 2p and N 1s spectra show the signatures of unidentified species (S $2p_{3/2}$ at 169 eV and N 1s at 399 eV).

dx.doi.org/10.1021/ja403082s | J. Am. Chem. Soc. 2013, 135, 9829−9842

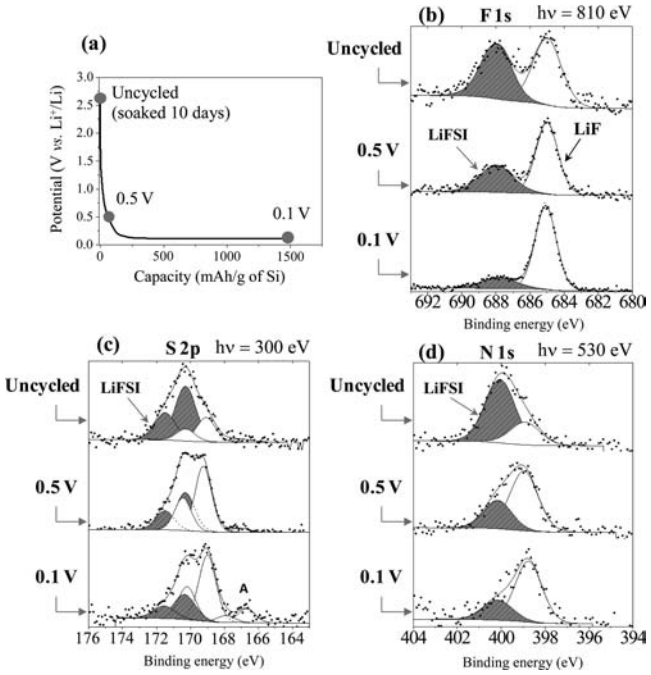

Figure 10. (a) First discharge of a Li//Si cell using LiFSI salt (current rate 150 mA·g^{-1} of Si, no precycling). The samples analyzed by PES are highlighted by gray points. (b) F 1s; (c) S 2p; and (d) N 1s spectra of the Si electrode upon the first discharge.

Upon the first discharge (i.e., reduction by lithium) the same components are observed, but the intensities of LiFSI peaks decrease gradually with respect to the peaks assigned to its degradation compounds. This displays a reduction mechanism of LiFSI at the surface of the electrode. Moreover, this mechanism takes place as soon as the first discharge, since the spectra obtained after discharge down to 0.1 V are rather close to those obtained after 50 or 100 cycles. Note that an additional component can be detected in S 2p spectra (peak A at ∼167 eV), but this one only results from degradation of LiFSI under the X-ray beam, since its intensity increases upon PES analysis time (already observed in Figure 9).

As shown previously, the lower sensitivity of LiFSI toward hydrolysis has a beneficial impact on the electrochemical performances of Li//Si batteries. Concerning its sensitivity toward reduction, LiFSI appears to be more easily reducible than $LiPF_6$ at the surface of the electrode, but this does not hamper a good electrochemical behavior, probably due to the formation of a protective layer at the surface of the electrode that prevents continuous reduction of the salt upon repeated discharges.

In the following part of this work we will study the electronic structure of LiFSI to better understand its reactivity and to try to understand this reduction mechanism occurring upon discharge.

3.4.2. DFT Calculations. In this study we calculated the monoelectronic energy levels and the coefficients of MOs of FSI^- ion, in order to investigate its electronic structure and its reactivity toward reduction (see Computational Details). The first step of this study was to validate the chosen model by simulating the XPS valence spectrum of LiFSI.

Figure 11 shows (a) the experimental valence spectrum of LiFSI (recorded with in-house XPS, hν = 1486.6 eV) and (b) the simulated spectrum. Previous works have shown that the contribution of Li^+ ion energy levels to the valence spectrum of

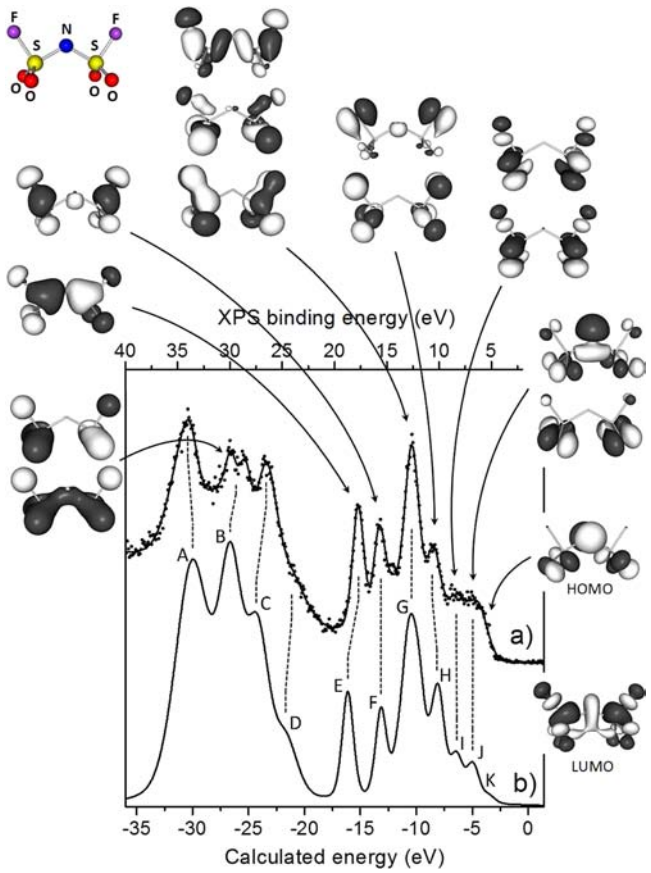

Figure 11. (a) Experimental (in-house XPS, hν = 1486.6 eV) and (b) calculated PES valence spectra of LiFSI. MOs of the FSI^- ion corresponding to energy levels have been represented (only selected MOs for peaks G–J).

such salts is negligible.[59] Therefore the valence spectrum of LiFSI consists of a series of peaks that can be interpreted by occupied MOs of the sole FSI^- ion. Three different models and geometries were considered for calculations: a simple FSI^- ion with (i) C_2 or (ii) C_{2v} geometry and (iii) an FSI^--Li^+ ion pair with C_s geometry (with Li^+ bidentately coordinated to one oxygen atom from each sulfonyl group), which was shown to be the most stable ion pair configuration by Scheers et al.[67] Geometry optimization was carried out in each case. Similar results were obtained for the three models, but the best simulation of XPS valence spectrum of LiFSI was obtained for the FSI^- ion model with C_{2v} geometry. Hence, the simulated valence spectrum and the corresponding MOs represented in Figure 11 are those obtained with this geometry.

In the valence spectrum of LiFSI, 11 components labeled A-K can be considered. Calculations results allowed us to assign peaks A, C, and D to MOs of sole F 2s, O 2s, and N 2s character, respectively, with a very low contribution of other AOs in each case. These three peaks have a strong atomic character. Peak B originates from two MOs of S 3s, O 2s, and F 2s (and also N 2s) characters, corresponding to S–O (and S–N) bonds in the molecule. The model is unable to account for the experimental splitting of peak B, which is probably due to differentiated environments of oxygen atoms in the solid phase. Peak E originates from one MO mainly involving bonding interactions between S 3s and N 2p AOs and can be considered as representative of S–N bonds. Peak F originates from one MO mainly involving bonding interactions between S 3s/3p

dx.doi.org/10.1021/ja403082s | J. Am. Chem. Soc. 2013, 135, 9829–9842

and F 2p AOs and is representative of S−F bonds. Peak G corresponds to five MOs (only three of them have been depicted), resulting from various bonding combinations of N 2p, S 3s/3p, O 2s/2p, and F 2p AOs and is therefore representative of S−N, S−F, and S−O bonds. Peak H corresponds to five MOs and peaks I and J correspond to four MOs each. These MOs are mainly of nonbonding F 2p, O 2p, and N 2p characters and can be attributed to fluorine, oxygen, and nitrogen "lone pairs" in the Lewis model. Finally, the weak shoulder labeled K corresponds to the HOMO, which is of dominant nonbonding N 2p character (nitrogen lone pair). It is not separated from peak J in the experimental spectrum.

As we can see in Figure 11, we obtain a very good correlation between experimental and simulated valence spectra of LiFSI, which validates the calculation method and the chosen model. In Figure 11 we also depicted the LUMO, which of course does not participate in the valence spectrum but is interesting because it acts as the electron acceptor if the FSI^- ion is reduced. The LUMO mainly results from a strong σ antibonding overlapping of S 3s/3p and F 2p AOs. A weak bonding overlapping of S 3s/3p and N 2s AOs and a weak π antibonding overlapping of S 3s/3p and O 2p AOs are also present. The acceptation of one electron in this MO will thus mainly result in the weakening of the S−F bond. Moreover, competition with another unoccupied MO can be excluded since the energy difference between the first and the second unoccupied MO is 0.89 eV according to our calculations. Therefore we can assume that reduction of the FSI^- ion will result in the break of S−F bonds. This is in good agreement with experimental PES observations (F 1s spectra in Figure 10) showing that the amount of LiF increases upon the first discharge (i.e., reduction), and ∼10−11 at. % of LiF was found at the surface of the electrode after 50−100 cycles. Moreover, the S 2p spectra recorded after discharge (see Figure 10) have revealed the presence of a degradation compound with an S $2p_{3/2}$ peak at 169 eV, which corresponds to a negative shift of −1.3 eV toward lower BE with respect to LiFSI. This is consistent with the loss of a very electronegative atom (fluorine) in the environment of sulfur. This may also explain the negative shift observed for N 1s spectra. As a result, the reduction of FSI^- at the electrode surface leads to the break of S−F bonds and to the formation of LiF. On the other hand, there is no evidence of a break of S−N bonds. Indeed, the S 2p/N 1s intensity ratio remains close to 2 upon cycling, while a decrease of this ratio would be expected if S−N bonds were broken due to the release of SO_2 gas. Note that the mechanism we propose here is rather different from that proposed by Huang et al.,[68] who have displayed the break of S−N bonds. However, their mechanism concerned the thermal decomposition of LiFSI at 180 °C. In our case we evidence the break of S−F bonds and the formation of LiF by electrochemical reduction.

4. CONCLUSION

In this study we have shown the beneficial role of LiFSI salt to improve the electrochemical performances of Li//Si cells. This beneficial role is mainly attributed to the interfacial reactivity of the silicon electrode vs the LiFSI-based electrolyte upon cycling. Especially, the much lower sensitivity of LiFSI toward hydrolysis with respect to $LiPF_6$ and its least tendency to form HF in the presence of traces of water is determinant.

By the use of depth-resolved PES analysis allowed by different X-ray photon energies we have shown that, unlike $LiPF_6$, long-term cycling with LiFSI does result neither in the fluorination of the electrode surface to form SiO_xF_y species from the surface oxide SiO_2 nor in the dissolution of the surface lithium oxide Li_2O. Instead, a continuous reaction process of SiO_2 with lithium upon cycling leads to the increase of lithium silicate Li_4SiO_4 at the surface of the electrode. Therefore, the favorable interactions between the binder and the active material surface are preserved.

The passivation layer (SEI) contains an organic and an inorganic part as it is commonly observed for carbonate-based liquid electrolytes. The same carbonaceous species are observed as when $LiPF_6$ is used as salt. A degradation mechanism of LiFSI salt at the surface of the electrode could be evidenced, and this mechanism does not hamper the good operation of the battery. As it occurs as soon as the first discharge (i.e., the first reduction), and because the amount of LiFSI degradation products increases only weakly after this first step, we believe these reduction products deposited at the surface of the electrode act as a passivation layer which prevents further reduction of the salt and preserves the electrochemical performances of the battery. Finally, this study opens the door to the study of other salts with lower fluorine contents than $LiPF_6$, in order to improve the stability of electrochemical performances upon cycling and address the safety issues due engendered by the presence of fluorine.

■ ASSOCIATED CONTENT

Supporting Information

Explanation of the increase in capacity observed for the first cycles of Li/Si cells showing discharge capacity vs cycle number (cycling between 0.12 and 0.9 V with a rate of 150 mA/g of Si) and potential vs capacity curves of the 1st, 5th, and 10th cycles. This material is available free of charge via the Internet at http://pubs.acs.org.

■ AUTHOR INFORMATION

Corresponding Author

remi.dedryvere@univ-pau.fr; kristina.edstrom@kemi.uu.se

Notes

The authors declare no competing financial interest.

■ ACKNOWLEDGMENTS

This work was carried out in the framework of ALISTORE European Research Institute. The authors are grateful to the European Community for financial support. The authors are also grateful to the French Education and Research Ministry and to StandUp for Energy, the Swedish Research Council VR and the Swedish Energy Agency.

■ REFERENCES

(1) Nagaura, T.; Tozawa, K.; in: *Progress in Batteries and Solar Cells*; JEC Press Inc.: Brunswick, OH, 1990; Vol. *9*, pp 209−217.
(2) Li, H.; Wang, Z.; Chen, L.; Huang, X. *Adv. Mater.* **2009**, *21*, 4593−4607.
(3) Scrosati, B.; Garche, J. r. *J. Power Sources* **2010**, *195*, 2419−2430.
(4) Larcher, D.; Beattie, S.; Morcrette, M.; Edström, K.; Jumas, J.-C.; Tarascon, J.-M. *J. Mater. Chem.* **2007**, *17*, 3759−3772.
(5) Kasavajjula, U.; Wang, C.; Appleby, A. J. *J. Power Sources* **2007**, *163*, 1003−1039.
(6) Obrovac, M. N.; Krause, L. J. *J. Electrochem. Soc.* **2007**, *154*, A103−A108.

(7) Wu, H.; Chan, G.; Choi, J. W.; Ryu, I.; Yao, Y.; McDowell, M. T.; Lee, S. W.; Jackson, A.; Yang, Y.; Hu, L.; Cui, Y. *Nat. Nanotechnol.* **2012**, *7*, 310−315.
(8) Evanoff, K.; Khan, J.; Balandin, A. A.; Magasinski, A.; Ready, W. J.; Fuller, T. F.; Yushin, G. *Adv. Mater.* **2012**, *24*, 533−537.
(9) Park, M.-H.; Kim, M. G.; Joo, J.; Kim, K.; Kim, J.; Ahn, S.; Cui, Y.; Cho, J. *Nano Lett.* **2009**, *9*, 3844−3847.
(10) Chen, H.; Dong, Z.; Fu, Y.; Yang, Y. *J. Solid State Electrochem.* **2009**, *14*, 1829−1834.
(11) Chan, C. K.; Peng, H.; Liu, G.; McIlwrath, K.; Zhang, X. F.; Huggins, R. A.; Cui, Y. *Nat. Nanotechnol.* **2008**, *3*, 31−35.
(12) Wu, H.; Zheng, G.; Liu, N.; Carney, T. J.; Yang, Y.; Cui, Y. *Nano Lett.* **2012**, *12*, 904−909.
(13) Liu, N.; Wu, H.; McDowell, M. T.; Yao, Y.; Wang, C.; Cui, Y. *Nano Lett.* **2012**, *12*, 3315−3321.
(14) Dalavi, S.; Pradeep, G.; Brett, L. L. *J. Electrochem. Soc.* **2012**, *159*, A642−A646.
(15) Nakai, H.; Kubota, T.; Kita, A.; Kawashima, A. *J. Electrochem. Soc.* **2011**, *158*, A798−A801.
(16) Choi, N.-S.; Yew, K. H.; Lee, K. Y.; Sung, M.; Kim, H.; Kim, S.-S. *J. Power Sources* **2006**, *161*, 1254−1259.
(17) Song, S.-W.; Baek, S.-W. *Electrochem. Solid-State Lett.* **2009**, *12*, A23−A27.
(18) Nguyen, C. C.; Song, S.-W. *Electrochim. Acta* **2010**, *55*, 3026−3033.
(19) Dudley, J. T.; Wilkinson, D. P.; Thomas, G.; LeVae, R.; Woo, S.; Blom, H.; Horvath, C.; Juzkow, M. W.; Denis, B.; Juric, P.; Aghakian, P.; Dahn, J. R. *J. Power Sources* **1991**, *35*, 59−82.
(20) Tarascon, J.-M.; Guyomard, D. *Solid State Ionics* **1994**, *69*, 293−305.
(21) Xu, K. *Chem. Rev.* **2004**, *104*, 4303−4418.
(22) Heider, U.; Oesten, R.; Jungnitz, M. *J. Power Sources* **1999**, *81*−*82*, 119−122.
(23) Campion, C. L.; Li, W.; Lucht, B. L. *J. Electrochem. Soc.* **2005**, *152*, A2327−A2334.
(24) Aurbach, D.; Markovsky, B.; Shechter, A.; Ein-Eli, Y.; Cohen, H. *J. Electrochem. Soc.* **1996**, *143*, 3809−3820.
(25) Plakhotnyk, A. V.; Ernst, L.; Schmutzler, R. *J. Fluorine Chem.* **2005**, *126*, 27−31.
(26) Hochgatterer, N. S.; Schweiger, M. R.; Koller, S.; Raimann, P. R.; Wohrle, T.; Wurm, C.; Winter, M. *Electrochem. Solid-State Lett.* **2008**, *11*, A76−A80.
(27) Munao, D.; van Erven, J. W. M.; Valvo, M.; Garcia-Tamayo, E.; Kelder, E. M. *J. Power Sources* **2010**, *196*, 6695−6702.
(28) Philippe, B.; Dedryvère, R.; Gorgoi, M.; Rensmo, H.; Gonbeau, D.; Edström, K. *Chem. Mater.* **2013**, *25*, 394−404.
(29) Kanamura, K.; Umegaki, T.; Shiraishi, S.; Ohashi, M.; Takehara, Z.-I. *J. Electrochem. Soc.* **2002**, *149*, A185−A194.
(30) Han, H.; Guo, J.; Zhang, D.; Feng, S.; Feng, W.; Nie, J.; Zhou, Z. *Electrochem. Commun.* **2011**, *13*, 265−268.
(31) Ishikawa, M.; Sugimoto, T.; Kikuta, M.; Ishiko, E.; Kono, M. *J. Power Sources* **2006**, *162*, 658−662.
(32) Paillard, E.; Zhou, Q.; Henderson, W. A.; Appetecchi, G. B.; Montanino, M.; Passerini, S. *J. Electrochem. Soc.* **2009**, *156*, A891−A895.
(33) Guerfi, A.; Duchesne, S.; Kobayashi, Y.; Vijh, A.; Zaghib, K. *J. Power Sources* **2008**, *175*, 866−873.
(34) Zaghib, K.; P. Charest, P.; Guerfi, A.; Shimb, J.; Perrier, M.; Striebel, K. *J. Power Sources* **2005**, *146*, 380−385.
(35) Li, L.; Zhou, S.; Han, H.; Li, H.; Nie, J.; Armand, M.; Zhou, Z.; Huang, X. *J. Electrochem. Soc.* **2011**, *158*, A74−A82.
(36) Han, H.-B.; Zhou, S.-S.; Zhang, D.-J.; Feng, S.-W.; Li, L.-F.; Liu, K.; Feng, W.-F.; Nie, J.; Li, H.; Huang, X.-J.; Armand, M.; Zhou, Z.-B. *J. Power Sources* **2011**, *196*, 3623−3632.
(37) Michot, C.; Armand, M.; Sanchez, J. Y.; Choquette, Y.; Gauthier, M. U.S. Patent US 5916475, 1999.
(38) Kang, S.-H.; Abraham, D. P.; Xiao, A.; Lucht, B. L. *J. Power Sources* **2008**, *175*, 526.
(39) Andersson, A. M.; Herstedt, M.; Bishop, A. G.; Edström, K. *Electrochim. Acta* **2002**, *47*, 1885−1898.
(40) Leroy, S.; Martinez, H.; Dedryvère, R.; Lemordant, D.; Gonbeau, D. *Appl. Surf. Sci.* **2007**, *253*, 4895.
(41) Li, J.; Lewis, R. B.; Dahn, J. R. *Electrochem. Solid-State Lett.* **2007**, *10*, A17.
(42) Obrovac, M. N.; Krause, L. J. *J. Electrochem. Soc.* **2007**, *154*, A103−A108.
(43) Oumellal, Y.; Delpuech, N.; Mazouzi, D.; Dupré, N.; Gaubicher, J.; Moreau, P.; Soudan, P.; Lestriez, B.; Guyomard, D. *J. Mater. Chem.* **2011**, *21*, 6201−6208.
(44) Shirley, D. A. *Phys. Rev. B* **1972**, *5*, 4709−4714.
(45) Scofield, J. H. *J. Electron Spectrosc. Relat. Phenom.* **1976**, *8*, 129−137.
(46) Gorgoi, M. *Nucl. Instrum. Methods Phys. Res., Sect. A* **2009**, *601*, 48.
(47) Schaefers, F.; Merlin, M.; Gorgoi, M. *Rev. Sci. Instrum.* **2007**, *78*, 123102.
(48) (a) Becke, A. D. *J. Chem. Phys.* **1993**, *98*, 5648. (b) Lee, C.; Yang, W.; Parr, R. G. *Phys. Rev. B* **1988**, *37*, 785.
(49) Frisch, M. J.; Trucks, G. W.; Schlegel, H. B.; Scuseria, G. E.; Robb, M. A.; Cheeseman, J. R.; Scalmani, G.; Barone, V.; Mennucci, B.; Petersson, G. A.; Nakatsuji, H.; Caricato, M.; Li, X.; Hratchian, H. P.; Izmaylov, A. F.; Bloino, J.; Zheng, G.; Sonnenberg, J. L.; Hada, M.; Ehara, M.; Toyota, K.; Fukuda, R.; Hasegawa, J.; Ishida, M.; Nakajima, T.; Honda, Y.; Kitao, O.; Nakai, H.; Vreven, T.; Montgomery, J. A., Jr.; Peralta, J. E.; Ogliaro, F.; Bearpark, M.; Heyd, J. J.; Brothers, E.; Kudin, K. N.; Staroverov, V. N.; Kobayashi, R.; Normand, J.; Raghavachari, K.; Rendell, A.; Burant, J. C.; Iyengar, S. S.; Tomasi, J.; Cossi, M.; Rega, N.; Millam, J. M.; Klene, M.; Knox, J. E.; Cross, J. B.; Bakken, V.; Adamo, C.; Jaramillo, J.; Gomperts, R.; Stratmann, R. E.; Yazyev, O.; Austin, A. J.; Cammi, R.; Pomelli, C.; Ochterski, J. W.; Martin, R. L.; Morokuma, K.; Zakrzewski, V. G.; Voth, G. A.; Salvador, P.; Dannenberg, J. J.; Dapprich, S.; Daniels, A. D.; Farkas, Ö.; Foresman, J. B.; Ortiz, J. V.; Cioslowski, J.; Fox, D. J. *Gaussian 09*, revision C.01; Gaussian, Inc.: Wallingford, CT, 2009.
(50) Varetto, U.; *Molekel 5.4.0.8*; Swiss National Supercomputing Centre: Lugano (Switzerland), 2009
(51) Gelius, U. In *Electron spectroscopy*; Shirley, D. A.Ed.; North-Holland: Amsterdam, 1972; p 311.
(52) Gelius, U. *J. Electron Spectrosc. Relat. Phenom.* **1974**, *5*, 985.
(53) Huang, J. T. J.; Rabalais, J. W. In *Electron Spectroscopy: theory, techniques and applications*; Brundle, C. R., Baker, A. D.,Eds.; Academic Press: New York, 1978.
(54) Dedryvère, R.; Leroy, S.; Martinez, H.; Blanchard, F.; Lemordant, D.; Gonbeau, D. *J. Phys. Chem. B* **2006**, *110*, 12986−12992.
(55) Philippe, B.; Dedryvère, R.; Allouche, J.; Lindgren, F.; Gorgoi, M.; Rensmo, H.; Gonbeau, D.; Edström, K. *Chem. Mater.* **2012**, *24*, 1107−1115.
(56) Tanuma, S.; Powell, C. J.; Penn, D. R. *Surf. Interface Anal.* **1991**, *17*, 911−926.
(57) Chang, W.-S.; Park, C.-M.; Kim, J.-H.; Kim, Y.-U.; Jeong, G.; Sohn, H.-J. *Energy Environ. Sci.* **2012**, *5*, 6895−6899.
(58) Guo, B.; Shu, J.; Wang, Z.; Yang, H.; Shi, L.; Liu, Y.; Chen, L. *Electrochem. Commun.* **2008**, *10*, 1876−1878.
(59) Dedryvère, R.; Gireaud, L.; Grugeon, S.; Laruelle, S.; Tarascon, J. M.; Gonbeau, D. *J. Phys. Chem. B* **2005**, *109*, 15868−15875.
(60) Bryngelsson, H.; Stjerndahl, M.; Gustafsson, T.; Edström, K. *J. Power Sources* **2007**, *174*, 970−975.
(61) Leroy, S.; Blanchard, F.; Dedryvère, R.; Martinez, H.; Carré, B.; Lemordant, D.; Gonbeau, D. *Surf. Interface Anal.* **2005**, *37*, 773−781.
(62) Peled, E.; Golodnitsky, D. In *Lithium-Ion Batteries: Solid-Electrolyte Interphase*; Balbuena, P. B., Wang, Y., Eds.; Imperial College Press: London, 2004.
(63) Peled, E. *J. Electrochem. Soc.* **1979**, *126*, 2047−2051.
(64) Aurbach, D.; Daroux, M. L.; Faguy, P. W.; Yeager, E. *J. Electrochem. Soc.* **1987**, *134*, 1611−1620.

(65) Hüfner, S. In *Photoelectron spectroscopy: principles and applications*; Springer-Verlag: Berlin, 1995.
(66) Scofield, J. H. In *Theoretical photoionization cross sections from 1 to 1500 keV*, Lawrence Livermore Lab report; University of California: Livermore, CA, 1973.
(67) Scheers, J.; Jónsson, E.; Jacobsson, P.; Johansson, P. *Electrochemistry* **2012**, *80*, 1825.
(68) Huang, J. H.; Hollenkamp, A. F. *J. Phys. Chem. C* **2010**, *114*, 21840−21847.